Universal Journal of Lasers, Optics, Photonics & Sensors (UJLOPS)
UINUJLOPS202306/W. Arrasmith[1], E. He[2]

Non-Diversity based, Software-Only, Atmospheric Turbulence Compensation (ATC) over Multiple Atmospheric Realizations using the Well-Optimized Linear Finder (WOLF) Methodology

W. Arrasmith[1], E. He[2]
[1]Florida Institute of Technology, Melbourne, FL, USA warrasmi@fit.edu, 321-674-8818
[2]Florida Institute of Technology, Melbourne, FL, USA ehe@fit.edu

ABSTRACT

The Well Optimized Linear Finder (WOLF) atmospheric turbulence compensation (ATC) methodology is currently a fast, software-dominant, diversity-based means to remove atmospheric turbulence from optical imagery and spectral imaging systems. One current drawback is that the WOLF ATC has been optimized to work with diversity-based imaging systems that require the simultaneous capture of both an in-focus image, and a diversity image that has its entrance pupil plane phase related in a known way to the in-focus image. Typically, the optical path length of the diversity image is changed relative to the in-focus image to generate this determinable phase difference at each entrance pupil plane sampled phase location. In this work, we present a method to use the WOLF ATC method using no extra hardware and eliminating the requirement for the simultaneously captured diversity image. This adaptation to the WOLF methodology provides a software-only ATC capability but instead requires multiple atmospheric realizations to determine the ATC image. Consequently, our WOLF adaptation is not considered real-time capable (faster than 30 Hz). In our software-based approach we first estimate the magnitude of the un-aberrated object spectrum, and subsequently estimate the associated object spectrum phase. This adaptation of the WOLF methodology can be directly extended to multi-spectral and/or hyperspectral imaging systems to generate spatial resolution and per pixel signal-to-noise ratio improvements for imagery at chosen wavelengths. Apart from providing an ATC capability for future imaging systems (both hyperspectral and high spatial-resolution imaging systems), the implication is that existing collected image data sets for general incoherent imaging systems that satisfy key collection requirements presented here, can potentially be retroactively corrected for atmospheric turbulence effects. We present the conceptual layout, technical approach, and provide simulated results. Although only two distinct narrow-band wavelengths are required for this WOLF adaptation, we demonstrate our results with a representative Hyperspectral Imaging (HSI) 'push-broom" imaging system application to show the generalization of our approach. Even though this WOLF adaptation may not be real time capable, it is highly scalable and dramatically benefits from general purpose parallel processing (GPPP) technology.

INTRODUCTION

When it comes to achieving high spatial resolution from an optical imaging system, the Earth's atmosphere presents the limiting factor for any well-designed optical system that has an entrance pupil plane diameter larger than the atmospheric coherence length ro.[1]
Solutions for mitigating atmospheric turbulence effects in imagery take one of the following three forms: 1) Adaptive Optics (AO) systems that are hardware intensive, bulky, costly, and real-time

capable, 2) Atmospheric Turbulence Compensation (ATC) imaging systems that are software-dominant, but are traditionally computationally slow, or 3) hybrid methods that blend AO and ATC capabilities and tend to perform somewhere in between AO and ATC imaging system implementations. [2,3,4] In this work, we focus on adapting a promising recently developed ATC capability so that it is more generally applicable to different types of imaging systems, such as color imaging cameras and multi-spectral/hyperspectral/ultra-spectral imaging systems. The WOLF ATC methodology provides a software-dominant, high-speed approach to remove aberrations due to atmospheric turbulence from optical imagery.[5] The WOLF methodology can provide real-time ATC (faster than 30 Hz) using a diversity-based imaging approach wherein an in-focus image and a diversity image are simultaneously captured as inputs to the WOLF ATC algorithm.[6] The current implementation of the WOLF methodology is software-dominant because it requires some hardware to produce the simultaneously captured in-focus and diversity image pair that are required as inputs to the WOLF algorithm. The hardware typically consists of beam splitters, narrow- band wavelength filters (one filter for monochromatic/grayscale images, two or three filters for color images, and more filters or prisms for spectral imaging systems), lenses, and a device for adjusting the optical path delay (OPD), along with image plane detectors.[5] Often, many of these components are already built into a basic imaging system, however, in diversity-based imaging systems, two optical paths are required to simultaneously capture the in-focus image and the related diversity image. In this work we demonstrate a method to remove the requirement for the diversity image so that only the in-focus image is needed. This eliminates the specialized hardware needed to produce the diversity image and adapts the WOLF methodology to work with regular (non-diversity-based) imaging systems. Image irradiance data must be captured at two or more distinct narrow-band wavelengths simultaneously and the method scales readily for HSI systems. The benefit of the third wavelength is that a second error metric can be generated that can isolate the correct entrance pupil plane phase estimate from 3 candidate estimates that otherwise would require dense sampling methods to determine the correct solution. Never-the-less, as will be seen below, if only two wavelengths are obtainable from the imaging system (such as some Quantum Well Photodetectors (QWPs), adaptive sampling methods can be used to determine the correct response. We provide the analytical framework for our adapted WOLF methodology and develop the mathematical formalism to illustrate our approach. We then use computer simulation to demonstrate how the WOLF methodology works and summarize our results.

ANALYSIS

The objective of our work herein is to provide an adaptation to the WOLF ATC method that removes the requirement for a diversity-image in the ATC process. This would greatly simplify the optical system component layout and make the WOLF ATC methodology available for a larger class of imaging systems (i.e., non-diversity-based imaging systems). Although irradiance data is required at only two distinct narrow- band wavelengths, a "push broom" hyperspectral imaging system is used as the conceptual model to show that our approach generalizes to imaging systems with an arbitrary number of wavelengths. The push broom HSI system is shown at the top-left of Figure 1. Only four representative wavelengths are shown in the figure even though HSI systems can have hundreds of wavelengths. In the push broom mode, the optical sensor maps a line of spatial pixels (shown oriented in the x – direction) wherein every pixel holds irradiance data at multiple wavelengths (shown as different colors in the figure). This array of spatial and spectral (wavelength) image data is moved in the negative y – direction to map out the so-called hypercube of the image data. In the second image from the top left, we see a 2D spatial array captured at one wavelength. This is representative of a monochromatic 2D imaging system, or it can be considered as one image at a given wavelength of the hyperspectral data cube. The bottom-left image in Figure

1 represents a HSI system that is capable of simultaneously capturing 2D spatial image data along with the spectral data for each pixel. The last image on the bottom right shows a step stair HSI configuration wherein the line of pixels changes wavelength at each subsequent increment along its progression along the negative y – axis. For the last HIS implementation on the bottom right, the WOLF methodology would also require one of the wavelengths to capture the full 2D spatial array. The WOLF ATC methods work for all these HSI implementations and more.

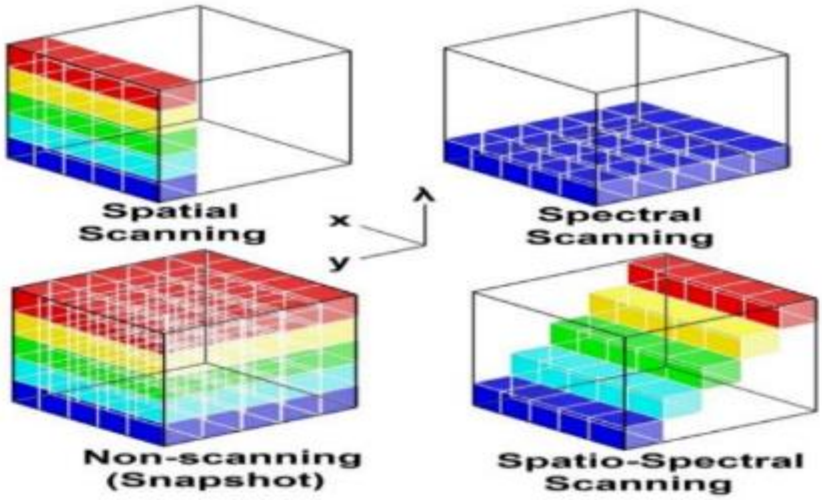

Figure 1 – Various Hyperspectral Imaging system implementation approaches [7]

In this work, the push-broom mode representative example provides a linear array of spatial pixel irradiance values that are simultaneously captured at each wavelength of the HSI system. There are a variety of physical mechanisms for producing this HSI data set using combinations of optical elements such as lenses, collimators, gratings, prisms, and rotating mechanisms, however, we focus on a general conceptual implementation to illustrate the fundamental mechanisms of the WOLF methodology, and consequently ignore HSI sensor implementation specific details.

To better understand the benefit of eliminating the diversity image from the ATC processing requirements, a general optical layout that includes the option for generating a diversity image, as well as the benefits of employing an aperture mask are illustrated in the conceptual layout shown in Figure 2. Note that the entrance pupil plane aperture masks shown at the bottom of Figure 2 provide benefit in computational speed for real-time WOLF ATC applications but aren't as important in this adaptation of the WOLF methodology since multiple realizations of the atmosphere are needed in this implementation, which tempers (although doesn't eliminate) the "need for speed" in this "no diversity" Concept of Operations (CONOPS). In Figure 2, we have a notional conceptual model that images a far-field object through atmospheric turbulence. The light is collected by the entrance pupil plane mirror (EPM) and collimated into a beam with the collimator (C1). The slit (S1) separates a linear array of pixels that are coming out of the page. In the entrance pupil plane, this corresponds to a line of spatial frequency components associated with a line of pixels across the object. For a diversity imaging system, the implementation of the imaging system requires two distinct optical paths wherein one path has a known diversity (such as a difference in the overall optical path length of the two paths that introduces a known defocus term in the entrance pupil plane phase). Figure 2 can readily be adapted for a diversity-based imaging system by 1) adding a lens after filter wheel 1 (FW1) so that we get the image at the detector (D1) instead of the entrance pupil plane irradiance, and 2) ensuring that the lengths of the two optical paths after the beam splitter (BS1) are different. The elimination of the diversity image requirement can remove the need for the second optical path (shown below the beam splitter (BS1) in Figure 2). Further, the proposed adaptation of the WOLF methodology does not require any entrance pupil plane aperture masks (shown as Ma1 and Ma2 in Figure 2) nor does it require the prism, or even the filter wheel if a detector is used that is sensitive to, and can distinguish between, multiple wavelengths at each pixel. Even the slit can be removed and consequently the 2D irradiance values can be simultaneously captured at the multi-wavelength capable detector. This is a dramatic simplification in the optical system layout and makes the WOLF methodology applicable to general 2D color imaging systems, yet still adaptable to systems with an arbitrary number of wavelengths at each spatial pixel. In our example, for brevity's sake, we use a push broom HSI architecture to illustrate our adaptation of the WOLF methodology to multi/hyperspectral imaging systems.

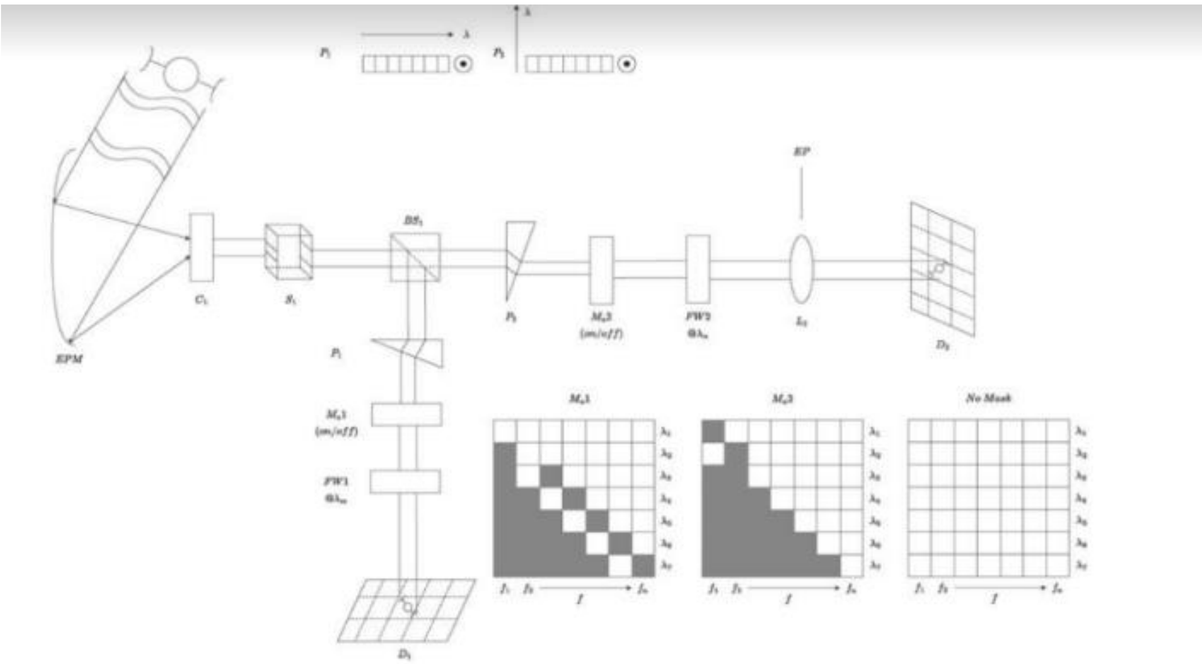

Figure 2 – Conceptual model for non-diversity based HSI system.

One benefit of having our object in the far-field of the imaging system is that we can use linear systems theory to mathematically describe the propagation of the electromagnetic field through the Earth's atmosphere. For an incoherent imaging system, the image irradiance can thereby be related to the object radiant emittance through a 2D spatial convolution with the imaging system's point spread function (PSF). In frequency space this becomes a point-wise multiplication given by, [8]

$$I^{\lambda_n}(\vec{f}) = O^{\lambda_n}(\vec{f})\mathcal{H}^{\lambda_n}(\vec{f}), \tag{1}$$

where for any given wavelength λ_n, $O^{\lambda_n}(\vec{f})$ represents the object radiant emittance spectrum, $\vec{f} = (f_y, f_x)$, is the 2D spatial frequency in the entrance pupil plane of the imaging systems, $\mathcal{H}^{\lambda_n}(\vec{f})$ is the Optical Transfer Function (OTF), and $I^{\lambda_n}(\vec{f})$ is the image irradiance spectrum at the same spatial frequency and center wavelength. We see from Equation (1) that we can recover the object radiant emittance spectrum by inverting the OTF and point-wise multiplying both sides of Equation (1) by the inverse of the OTF.

The WOLF methodology will be used to determine the OTF from estimates of the entrance pupil plane phase aberrations due to the atmosphere. To accomplish this, we need a mathematical expression for the OTF in terms of entrance pupil plane phase parameters. Equation (2) provides an expression for the OTF in terms of $W^{\lambda_n}(\vec{f})$, the Generalized Pupil Function (GPF),

$$\mathcal{H}^{\lambda_n}(\vec{f}) = \frac{W^{\lambda_n}(\vec{f}) \otimes W^{\lambda_n}(\vec{f})}{N_{ep}}, \tag{2}$$

where Nep is the number of entrance pupil plane sample points for the HSI push broom imaging system. The ⊗ symbol is the 2D autocorrelation of the GPF in frequency space, and the GPF is given by,

$$W^{\lambda_n}(\vec{f}) = A(\vec{f})e^{j\theta^{\lambda_n}(\vec{f})}. \tag{3}$$

In Equation (3) the amplitude function A(f⃗) is typically set to one inside the clear aperture of the entrance pupil and zero outside of the aperture. This is because for many imaging systems that have the entrance pupil plane within the Earth’s atmosphere, the atmospheric phase aberrations dominate, and the amplitude effects can safely be ignored. Some exceptions to the phase-only aberration assumption are due to distributed turbulence effects and/or strong scintillation effects such as in high energy laser systems. In Equation (3) the atmospheric phase aberrations are modeled by the entrance pupil plane phases θ λn(f⃗), which are functions of wavelength, and are located at a particular physical location in the entrance pupil, but are associated with a spatial frequency that is fundamental to the OTF in Equation (1). The relationship between the spatial coordinate and the spatial frequency coordinate scales as x⃗ = λndif⃗ where di is the imaging system’s effective focal length. In Equation (2) we see that the OTF is the 2D autocorrelation of the GPF which traditionally can be quite computationally slow and so Fourier-based methods are commonly employed to estimate the OTF. However, the WOLF methodology has improved upon the traditional correlation-based approach by 1) requiring no more than 2 complex exponential phase difference with only two entrance pupil plane unknown phases and complex constant to be calculated instead of potentially millions of complex exponential phase differences, 2) exploiting redundancies in the entrance pupil plane phases as related to the OTF, 3) taking advantage of inherent symmetries in the OTF, 4) allowing for the incorporation of parallel processing methods, and 5) employing optimization strategies in combining entrance pupil plane phases. These five attributes make the WOLF methodology highly competitive with traditional ATC methods and offers a faster and more accurate approach for removing atmospheric turbulence from incoherent imaging systems. In our approach we have also assumed unit magnification throughout and defer the inclusion of magnification parameters to specific implementations of the optical system as is conventionally done. Another assumption that we employ is that the Taylor’s frozen flow approximation applies, which assumes that the atmosphere changes on the order of a few milliseconds. Consequently, the integration time of the optical sensors cannot exceed a few milliseconds without risking a change to the state of the atmospheric aberrations. We assume a frozen atmospheric state for integration times up to 2 ms. In this paper, we develop a non-diversity-based push broom HSI system without the requirement for any specialized ATC hardware such as aperture masks or simultaneously captured images with different optical path lengths. We evaluate the conceptual layout in Figure 2 using the entrance pupil on the far bottom-right (no aperture mask). Using this open cell entrance pupil plane cell structure that passes the electromagnetic wave at all cell locations, we see that for the 1-point overlap condition with two different wavelengths selected for the differing optical paths in Figure 2, we get the same result as if the masks were turned on. [9] Therefore, the same procedure as for a masked 1-point overlap approach can be used to select θi λ1 and estimate θj λ1 through the WOLF-Tau sub-algorithm, to carry out the ATC on the HSI 1-point overlap data set.[9] The resulting WOLF-Tau outputs are, the object radiant emittance spectrum O1 λn (l (Nep) , fl=1), values of θj λn at all HSI wavelengths (or wavelengths of interest), the value of the OTF at all wavelengths of interest H1 λn (l(Nep) ,fl=1), and we assume that the irradiance spectrum for each isolated wavelength and linear array element is available from the push-broom HSI system collected data set. In the above WOLF-Tau outputs, the subscript 1 refers to the 1 – point overlap, the coordinate l is an index that runs over the available wavelengths, θi λ1is the entrance pupil plane phase aberration at the first element of the HSI push broom entrance pupil plane linear array at the first wavelength, θjλ1 is the last element of the HSI push broom entrance pupil plane linear array at the first wavelength, and Nep is the number of entrance pupil plane samples in the linear push broom array at one wavelength. Once the 1-point overlap process is complete and we have both θi λn and θj λn available at all wavelengths of interest, we need to estimate the object radiant emittance magnitude for the cases of overlaps greater than 1 (i.e., for the cases where k > 1). If we look at the general expression for the irradiance spectrum at a given wavelength we get, [5]

$$I_k^{\lambda_n}\left(l_{(N_{ep})}, f_{l=k}\right) = O_k^{\lambda_n}\left(l_{(N_{ep})}, f_{l=k}\right)\mathcal{H}_k^{\lambda_n}\left(l_{(N_{ep})}, f_{l=k}\right) = \left|O_k^{\lambda_n}\left(l_{(N_{ep})}, f_{l=k}\right)\right| e^{j\theta_o^{\lambda_n}\left(l'_{(N_{ep})}, f_{l=k}\right)}\left[\frac{e^{j\left(\Delta\theta_{i,s}^{\lambda_n}\right)}+C_k^{\lambda_n}+e^{j\left(\Delta\theta_{r,j}^{\lambda_n}\right)}}{N_{ep}}\right]. \tag{4}$$

We note that Equation (4) is also valid for the 2-point overlap case ($k = 2$) if the complex constant $C_k^{\lambda_n}$ is set to zero. By inspecting Equation (4), we notice that 1) the complex constant $C_k^{\lambda_n}$ is determinable based on previous overlap results, and 2) the terms inside the square brackets at the right side of Equation (4) are in fact the OTF itself. If we loosely write the OTF part of Equation (4) as a magnitude and phase component, but keep the explicit terms as shown in Equation (4), we get for the OTF,

$$\mathcal{H}_k^{\lambda_n}\left(l_{(N_{ep})}, f_{l=k}\right) = \left|\mathcal{H}_k^{\lambda_n}\left(l_{(N_{ep})}, f_{l=k}\right)\right| e^{j\sphericalangle\left(\mathcal{H}_k^{\lambda_n}\left(l_{(N_{ep})}, f_{l=k}\right)\right)}, \tag{5a}$$

where,

$$\left|\mathcal{H}_k^{\lambda_n}\left(l_{(N_{ep})}, f_{l=k}\right)\right| = \left|\left[\frac{e^{j\left(\Delta\theta_{i,s}^{\lambda_n}\right)}+C_k^{\lambda_n}+e^{j\left(\Delta\theta_{r,j}^{\lambda_n}\right)}}{N_{ep}}\right]\right|, \tag{5b}$$

and,

$$\Theta_{\mathcal{H};k}^{\lambda_n}\left(l_{(N_{ep})}, f_{l=k}\right) = \sphericalangle\left(\mathcal{H}_k^{\lambda_n}\left(l_{(N_{ep})}, f_{l=k}\right)\right) = \sphericalangle\left(\left[\frac{e^{j\left(\Delta\theta_{i,s}^{\lambda_n}\right)}+C_k^{\lambda_n}+e^{j\left(\Delta\theta_{r,j}^{\lambda_n}\right)}}{N_{ep}}\right]\right), \tag{5c}$$

where the symbol $\sphericalangle$ means taking the angle of the expression inside the parentheses in radians. Upon substituting Equations (5b) and (5c) into Equation (4) and collecting terms, we get,

$$I_k^{\lambda_n}\left(l_{(N_{ep})}, f_{l=k}\right) = O_k^{\lambda_n}\left(l_{(N_{ep})}, f_{l=k}\right)\mathcal{H}_k^{\lambda_n}\left(l_{(N_{ep})}, f_{l=k}\right) =$$
$$\left|O_k^{\lambda_n}\left(l_{(N_{ep})}, f_{l=k}\right)\right|\left|\mathcal{H}_k^{\lambda_n}\left(l_{(N_{ep})}, f_{l=k}\right)\right| e^{j\left(\theta_o^{\lambda_n}\left(l'_{(N_{ep})}, f_{l=k}\right)+\Theta_{\mathcal{H};k}^{\lambda_n}\left(l_{(N_{ep})}, f_{l=k}\right)\right)}. \tag{6}$$

If we take the magnitude of the irradiance spectrum, we end up with the following expression,

$$\left|I_k^{\lambda_n}\left(l_{(N_{ep})}, f_{l=k}\right)\right| = \left|O_k^{\lambda_n}\left(l_{(N_{ep})}, f_{l=k}\right)\right|\left|\mathcal{H}_k^{\lambda_n}\left(l_{(N_{ep})}, f_{l=k}\right)\right| = \left|O_k^{\lambda_n}\left(l_{(N_{ep})}, f_{l=k}\right)\right|\left|\frac{e^{j\left(\Delta\theta_{i,s}^{\lambda_n}\right)} + C_k^{\lambda_n} + e^{j\left(\Delta\theta_{r,j}^{\lambda_n}\right)}}{N_{ep}}\right|. \quad (7)$$

Inspecting the bracketed term on the right, we see that it is a function of the determinable complex constant $C_k^{\lambda_n}$ and two unknown phases $\theta_r^{\lambda_n}$ and $\theta_s^{\lambda_n}$ (since we determined $\theta_i^{\lambda_n}$ and $\theta_j^{\lambda_n}$ from the 1-point overlap scenario using the WOLF-Tau sub-algorithm). If we now break the ATC problem into two parts, first estimating the object magnitude $\left|O_k^{\lambda_n}\left(l_{(N_{ep})}, f_{l=k}\right)\right|$ at two wavelengths, and then estimating the unknown phases $\theta_r^{\lambda_n}$ and $\theta_s^{\lambda_n}$ through minimization of an error metric, we can recover the ATC object radiant emittance. To estimate the object magnitude for a $2-$point overlap in a given linear direction, at a given wavelength $\left|O_2^{\lambda_n}\left(l_{(N_{ep})}, f_{l=2}\right)\right|$ we first relax the single snapshot requirement and allow for the atmosphere to change its state. Looking at the OTF component in Equation (7), we note that as the atmosphere changes, the arguments of the two complex exponentials randomly change and the complex constant $C_k^{\lambda_n}$ changes too. For the 2-point overlap case, the complex constant is zero and only the entrance pupil plane phases in the complex exponentials change randomly as the atmosphere changes states (on the order of milliseconds). If both complex exponential phase differences fortuitously sum to zero because of the atmospheric phase fluctuations at the same time, then the complex exponential terms inside the OTF are maximized. Therefore, for the 2-point overlap case, we can take many samples of the irradiance spectrum magnitude $\left|I_2^{\lambda_n}\left(l_{(N_{ep})}, f_{l=2}\right)\right|$ and use the largest irradiance spectrum magnitude value to estimate the object radiant emittance spectrum magnitude, $\left|O_2^{\lambda_n}\left(\widehat{l_{(N_{ep})}}, f_{l=2}\right)\right|$ from,

$$\left|O_2^{\lambda_n}\left(\widehat{l_{(N_{ep})}}, f_{l=2}\right)\right| = \frac{N_{ep}\left|I_2^{\lambda_n}\left(l_{(N_{ep})}, f_{l=2}\right)\right|_{max}}{2}, \quad (8)$$

where the ^ symbol on the left denotes the estimated value. There are of course no guarantees that the true maximum value of |I2 λn (l(Nep) , fl=2)| has been reached, and that the arguments of the complex exponentials in Equation (7) both sum to zero, but the larger the value of |I2 λn(l (Nep), fl=2)|, the closer we are to this condition being true. For this method to work, the underlying object that is being observed cannot change its magnitude or phase throughout the observational period (such as a fixed object with respect to the observational platform imaged at millisecond exposures over many realizations of the atmosphere. With regards to the 3 (or more) point overlap scenario in which the complex constant is not zero, we note that from Equation (4) that Ck λn is a sum of complex exponential phase differences that have an upper limit that is equal to the number of terms in the complex exponential sum (which is k – 2). It is also fortuitous that we can determine the complex constant Ck λn analytically and deterministically for each atmospheric realization, aided by our previous overlap results (i.e., new values of entrance pupil plane phases and OTF values for new atmospheric realizations can be quickly determined using previous overlap (k-1) results since the object radiant emittance spectrum has been determined and doesn't change per our assumptions). This allows us to establish what the maximum (or minimum) irradiance spectrum magnitude value on the left side of Equation (7) is with respect to the complex constant Ck λn. We hope to use this maximum (or minimum) value of the irradiance spectrum magnitude to identify the condition when the random fluctuations of the atmospheric phases in the complex exponentials of the OTF in Equation (7) sum to approximately zero thereby permitting the determination of the object radiant emittance spectrum magnitude estimate from

$$\left|O_k^{\lambda_n}\left(\widehat{l_{(N_{ep})}}, f_{l=k}\right)\right| = \frac{N_{ep}\left|I_k^{\lambda_n}\left(l_{(N_{ep})}, f_{l=k}\right)\right|_{max}}{\left|2+C_k^{\lambda_n}\right|}. \quad (9)$$

By inspecting Equation (7), it becomes immediately apparent that whether the measured irradiance spectrum magnitude value is maximum, minimum, or somewhere in between depends largely on the real and imaginary parts of the complex constant $C_k\ \lambda_n$ which is determinable with some tedium, but changes for every different instantiation of the atmosphere, as well as different values of k. To further complicate measures, the irradiance spectrum magnitude in Equation (7) is maximized (or minimized) relative to $C_k\ \lambda_n$ for the following paired phase difference realizations: $\{\Delta\theta_{i,s}\ \lambda_n, \Delta\theta_{r,j}\ \lambda_n\} = \{0,0\}, \{-\pi, \pi\}, \{\pi\ 2, \pi\ 2\}$, $\{-\pi\ 2, -\pi 2\}$, and equivalent angles such as $\{\pi, -\pi\}$, $\{-3\pi 2, -3\pi\ 2\}$, $\{+3\pi 2+3\pi\ 2\}$ and other phase difference combinations that lead to identical paired phase difference realizations that are both 0, $\pi/2$, π, or $3\pi/2$, or equivalent. These paired phase difference realizations will lead to maximum or minimum values of $|I_k\ \lambda_n\ (l(N_{ep}), f_l=k)|$ depending on the value of the real and imaginary parts of the complex constant $C_k\ \lambda_n$. Note that if the real part of the complex constant $C_k\ \lambda_n$ is positive and, through the statistical variations of the atmospheric phases in the OTF term sum to zero (i.e., $\{\Delta\theta_{i,s}\ \lambda_n, \Delta\theta_{r,j}\ \lambda_n\} = \{0,0\}$), then the sum of the complex exponentials on the right side of Equation (7) equals 2, and we expect the magnitude of the OTF to be maximized. However, if the real part of the complex constant $C_k\ \lambda_n$ is negative, then the sum of the positive 2 and negative real part of $C_k\ \lambda_n$ produces a smaller net magnitude than what would have been attained if the real part of $C_k\ \lambda_n$ where positive. To proceed, we need to pick one of these phase difference pairings such as $\{\Delta\theta_{i,s}\ \lambda_n, \Delta\theta_{r,j}\ \lambda_n\} = \{0,0\}$), and properly account for the effects of the other possible paired phase difference realizations that counter the maximization of $|I_2\ \lambda_n\ (l(N_{ep}), f_l=2)|$ (namely, the equivalent/similar entrance pupil plane phase combinations of $\{\Delta\theta_{i,s}\ \lambda_n, \Delta\theta_{r,j}\ \lambda_n\} = \{-\pi, \pi\}, \{\pi, -\pi\}, \{\pi\ 2, -\pi\ 2\}$, $\{-\pi\ 2, \pi\ 2\}$) so that the form of the equation in the denominator of Equation (9) doesn't change for maximum values of our observable, $|I_k\ \lambda_n\ (l(N_{ep}), f_l=k)|$. For example, if for aparticular atmospheric realization, the paired entrance pupil plane phase differences are $\{\Delta\theta_{i,s}\ \lambda_n, \Delta\theta_{r,j}\ \lambda_n\} = \{-\pi, \pi\}$, then from Equation (7) and (9) we see that the denominator on the right side of Equation (9) becomes $|-2 + C_k\ \lambda_n\ |$. This would lead to a slightly different object estimator in Equation (9). Table 1 shows some of the possible combinations of paired phase difference results that would maximize or minimize the

Table 1: Parameter relationships in estimating $\left|I_k^{\lambda_n}\left(l_{(N_{ep})}, f_{l=k}\right)\right|_{max,min}$ with associated error function.

$\Delta\theta_{i,s}^{\lambda_n}$	$\Delta\theta_{r,j}^{\lambda_n}$	$C_{k;r}^{\lambda_n}$	$C_{k;i}^{\lambda_n}$	Estimation Function	$\left|I_k^{\lambda_n}\left(l_{(N_{ep})}, f_{l=k}\right)\right|_{max,min}$	Estimation Function	$\left|I_k^{\lambda_n}\left(l_{(N_{ep})}, f_{l=k}\right)\right|$
0	0	Pos	Pos	$\left|2+C_k^{\lambda_n}\right|$	max	$\left|-2+C_k^{\lambda_n}\right|$	min
0	0	Pos	Neg	$\left|2+C_k^{\lambda_n}\right|$	max	$\left|-2+C_k^{\lambda_n}\right|$	min
0	0	Neg	Pos	$\left|2+C_k^{\lambda_n}\right|$	min	$\left|-2+C_k^{\lambda_n}\right|$	max
0	0	Neg	Neg	$\left|2+C_k^{\lambda_n}\right|$	min	$\left|-2+C_k^{\lambda_n}\right|$	max
π	π	Pos	Pos	$\left|2+C_k^{\lambda_n}\right|$	min	$\left|-2+C_k^{\lambda_n}\right|$	max
π	π	Pos	Neg	$\left|2+C_k^{\lambda_n}\right|$	min	$\left|-2+C_k^{\lambda_n}\right|$	max
π	π	Neg	Pos	$\left|2+C_k^{\lambda_n}\right|$	max	$\left|-2+C_k^{\lambda_n}\right|$	min
π	π	Neg	Neg	$\left|2+C_k^{\lambda_n}\right|$	max	$\left|-2+C_k^{\lambda_n}\right|$	min
$\frac{\pi}{2}$	$\frac{\pi}{2}$	Pos	Pos	$\left|2+C_k^{\lambda_n}\right|$	max	$\left|-2+C_k^{\lambda_n}\right|$	min
$\frac{\pi}{2}$	$\frac{\pi}{2}$	Pos	Neg	$\left|2+C_k^{\lambda_n}\right|$	min	$\left|-2+C_k^{\lambda_n}\right|$	max
$\frac{\pi}{2}$	$\frac{\pi}{2}$	Neg	Pos	$\left|2+C_k^{\lambda_n}\right|$	max	$\left|-2+C_k^{\lambda_n}\right|$	min
$\frac{\pi}{2}$	$\frac{\pi}{2}$	Neg	Neg	$\left|2+C_k^{\lambda_n}\right|$	min	$\left|-2+C_k^{\lambda_n}\right|$	max
$-\frac{\pi}{2}$	$-\frac{\pi}{2}$	Pos	Pos	$\left|2+C_k^{\lambda_n}\right|$	min	$\left|-2+C_k^{\lambda_n}\right|$	max
$-\frac{\pi}{2}$	$-\frac{\pi}{2}$	Pos	Neg	$\left|2+C_k^{\lambda_n}\right|$	max	$\left|-2+C_k^{\lambda_n}\right|$	min
$-\frac{\pi}{2}$	$-\frac{\pi}{2}$	Neg	Pos	$\left|2+C_k^{\lambda_n}\right|$	min	$\left|-2+C_k^{\lambda_n}\right|$	max
$-\frac{\pi}{2}$	$-\frac{\pi}{2}$	Neg	Neg	$\left|2+C_k^{\lambda_n}\right|$	max	$\left|-2+C_k^{\lambda_n}\right|$	min

observable $\left|I_k^{\lambda_n}\left(l_{(N_{ep})}, f_{l=k}\right)\right|$, as a function of attributes of the complex constant $C_k^{\lambda_n}$, and required expression in the right-side denominator estimation function in Equation (9). From Table 1, if we want to use the entrance pupil plane phase difference pairings $\left\{\Delta\theta_{i,s}^{\lambda_n}, \Delta\theta_{r,j}^{\lambda_n}\right\} = \{0,0\}$) to correspond to a maximum value of the observable $\left|I_k^{\lambda_n}\left(l_{(N_{ep})}, f_{l=k}\right)\right|$, then contributions from other possible entrance pupil plane phase difference pairings that potentially maximize the observable $\left|I_k^{\lambda_n}\left(l_{(N_{ep})}, f_{l=k}\right)\right|$, but require another estimation function (i.e., other than $\left|2+C_k^{\lambda_n}\right|$) must be processed so that there is no ambiguity in the needed estimation function at the right-side bottom of Equation (9). This can be done by grouping terms relative to the sign on the real and imaginary parts of the complex constant $C_k^{\lambda_n}$ which is known. For instance, if the sign on the real part of the complex constant $C_{k;r}^{\lambda_n}$ is positive, and also the sign on the imaginary part of $C_{k;i}^{\lambda_n}$ is positive, then for $\left\{\Delta\theta_{i,s}^{\lambda_n}, \Delta\theta_{r,j}^{\lambda_n}\right\} = \{0,0\}$ the observable $\left|I_k^{\lambda_n}\left(l_{(N_{ep})}, f_{l=k}\right)\right|$ will be maximum using the estimation function $\left|2+C_k^{\lambda_n}\right|$. Note that, for positive real and imaginary parts of the complex constant $C_k^{\lambda_n}$, $\left|I_k^{\lambda_n}\left(l_{(N_{ep})}, f_{l=k}\right)\right|$ will also be maximized for $\left\{\Delta\theta_{i,s}^{\lambda_n}, \Delta\theta_{r,j}^{\lambda_n}\right\} = \left\{\frac{\pi}{2}, \frac{\pi}{2}\right\}$ (or equivalent phase combinations). This is not an issue since the error function $\left|2+C_k^{\lambda_n}\right|$ is the same for both paired entrance pupil plane phase difference cases, and Equation (9) is equally valid for estimating the object radiant emittance spectrum. All other realization of $\left|I_k^{\lambda_n}\left(l_{(N_{ep})}, f_{l=k}\right)\right|$ as the entrance pupil plane phase differences change due to variations in the atmosphere, where $\left\{C_{k;r}^{\lambda_n}, C_{k;i}^{\lambda_n}\right\} = \{positive, positive\}$ result in instantiations of the observable $\left|I_k^{\lambda_n}\left(l_{(N_{ep})}, f_{l=k}\right)\right|$ that are less than the maximum value. Consequently, for positive values of the real and imaginary part of the complex constant, we can search for the maximum value of the observable imaginary part of the complex constant, we can search for the maximum value of the observable $I_k^{\lambda_n}\left(l_{(N_{ep})}, f_{l=k}\right)$, and then use Equation (9) to estimate the object radiant emittance spectrum. For other combinations of the sign of the real and imaginary parts of the complex constant, where $\left\{C_{k;r}^{\lambda_n}, C_{k;i}^{\lambda_n}\right\} \neq \{positive, positive\}$, these can either be ignored in the search for the maximum value of $\left|I_k^{\lambda_n}\left(l_{(N_{ep})}, f_{l=k}\right)\right|$, or separate searches using different estimation functions (as in the denominator of Equation (9)), for differing combinations of signs on the real and imaginary parts of $C_k^{\lambda_n}$ can be established to complement the $\left\{C_{k;r}^{\lambda_n}, C_{k;i}^{\lambda_n}\right\} = \{positive, positive\}$ results. For example, if $\left\{C_{k;r}^{\lambda_n}, C_{k;i}^{\lambda_n}\right\} = \{negative, negative\}$, there are two values of paired entrance pupil plane phase differences that also lead to a maximum value of $\left|I_k^{\lambda_n}\left(l_{(N_{ep})}, f_{l=k}\right)\right|$ and that use the same estimation function $\left|2 + C_k^{\lambda_n}\right|$. From Table 1, these paired entrance pupil plane phase difference values are $\left\{\Delta\theta_{i,s}^{\lambda_n}, \Delta\theta_{r,j}^{\lambda_n}\right\} = \left\{-\frac{\pi}{2}, -\frac{\pi}{2}\right\}$ and, $\left\{\Delta\theta_{i,s}^{\lambda_n}, \Delta\theta_{r,j}^{\lambda_n}\right\} = \{\pi, \pi\}$, or equivalents. The object radiant emittance spectrum magnitude in Equation (9) can then be estimated for the $k = 3$ (or more) overlap cases from Equation (9). We used computer simulation to demonstrate the case for $\left\{C_{k;r}^{\lambda_n}, C_{k;i}^{\lambda_n}\right\} = \{positive, positive\}$ and assumed (as is practical) that the complex quantity can be determined for every atmospheric realization as needed. We generated 1000 different atmospheric realizations where the entrance pupil plane phases ($\theta_i^{\lambda_n}$, $\theta_j^{\lambda_n}$, $\theta_r^{\lambda_n}$, and $\theta_s^{\lambda_n}$) in the complex exponentials in Equation (4) were random draws from a uniform distribution over their principal range ($-\pi$, π]).[10] Monte Carlo simulation was then used to generate various realizations of the irradiance spectrum, and Equation (9) was used to estimate the magnitude of the object radiant emittance spectrum $\left|O_k^{\lambda_n}\left(\widehat{l_{(N_{ep})}, f_{l=k}}\right)\right|$ for various realizations of the atmosphere (i.e., different random draws of the entrance pupil plane phases). For each random realization of the irradiance spectrum magnitude in Equation (7), the maximum value was kept for positive real and imaginary parts of values of $C_k^{\lambda_n}$. We repeated 25 trials, each with 1000 atmospheric realizations to generate random realizations of the irradiance spectrum in Equation (4) at two separate wavelengths. Equation (9) was used to estimate the objects radiant emittance spectrum magnitude at both wavelengths and compared to "truth" (reference) object radiant emittance spectrum magnitude values. The mean value of our estimate $\left|O_{k>2}^{\lambda_1}\left(\widehat{l_{(N_{ep})}, f_{l=k>2}}\right)\right|$ was 5.01 and our truth value was 5.0. The variance was 0.089. For the second wavelength, the mean of our estimate $\left|O_{k>2}^{\lambda_2}\left(l_{(N_{ep})}, f_{l=k>2}\right)\right|$ was 3.794 and our truth value was 3.883. The variance was 0.071. There appears to be a reasonable agreement between the truth and estimated values of the object radiant emittance spectrum magnitude for both wavelengths. This procedure can be used to estimate the object radiant emittance spectrum magnitude at any two wavelengths and for any number of overlaps k. The equation $\lambda_n \theta_x^{\lambda_n} = \lambda_m \theta_x^{\lambda_m}$, where the dummy variable x represents an arbitrary entrance pupil plane phase linear array index identifier, can be used to scale the entrance pupil plane results to any other wavelength of interest. By inspecting the irradiance spectrum magnitude in Equation (7), we see that the right side of the equation becomes a function of only 2 unknown variables, $\theta_r^{\lambda_n}$ and $\theta_s^{\lambda_n}$, for any value of overlaps $k \geq 2$, recall that $\theta_i^{\lambda_n}$ and $\theta_j^{\lambda_n}$ are determined from the 1-point overlap process discussed above. We now only need to solve for $\theta_r^{\lambda_n}$ and $\theta_s^{\lambda_n}$ by finding a suitable error metric that minimizes only upon the correct choice of $\theta_r^{\lambda_n}$ and $\theta_s^{\lambda_n}$, and the related entities $\theta_r^{\lambda_m}$ and $\theta_s^{\lambda_m}$. For example, using Equation (7), the following error metric that we developed,

$$E_{k;(r,s)}^{\lambda_n,\lambda_m}\left(l'_{(N)}, f_k\right) = \left|\frac{\left|I_k^{\lambda_m}(l'_N, f_k)\right|}{\left|I_k^{\lambda_n}(l'_N, f_k)\right|} - \frac{\left|O_k^{\lambda_m}(l'_N, f_k)\right|}{\left|O_k^{\lambda_n}(l'_N, f_k)\right|} \frac{\left|e^{j\left(\Delta\theta_{i,s}^{\lambda_m}\right)} + C_k^{\lambda_m} + e^{j\left(\Delta\theta_{r,j}^{\lambda_m}\right)}\right|}{\left|e^{j\left(\Delta\theta_{i,s}^{\lambda_n}\right)} + C_k^{\lambda_n} + e^{j\left(\Delta\theta_{r,j}^{\lambda_n}\right)}\right|}\right|, \quad (10)$$

goes to zero only for the correct choice of $\theta_r^{\lambda_n}$ and $\theta_s^{\lambda_n}$, and the relatable, through $\lambda_n\theta_x^{\lambda_n} = \lambda_m\theta_x^{\lambda_m}$, $\theta_r^{\lambda_m}$ and $\theta_s^{\lambda_m}$. The error metric in Equation (10) was checked for 1000 different atmospheric realizations and, with correct phase estimates of $\theta_r^{\lambda_n}$ and $\theta_s^{\lambda_n}$ at both wavelengths of interest, the simulation produced error magnitudes less than 1 x 10^{-15}. By keeping 3 of the 4 phases accurate, and only varying one phase by about 22% off the correct value, the minimum error increased by 9 orders of magnitude, showing that the error metric does not go to zero for incorrect estimates of even just one of the entrance pupil plane phases (all others estimated correctly). Figure 3 shows the error minimization function in Equation (10) plotted as a function of one of its estimated parameters $\theta_r^{\lambda_n}$ over its principal range (-π, π]. This is a nice smooth function with a clear minimum over the search space. We only need 2 wavelengths to use Equation (10, 23).

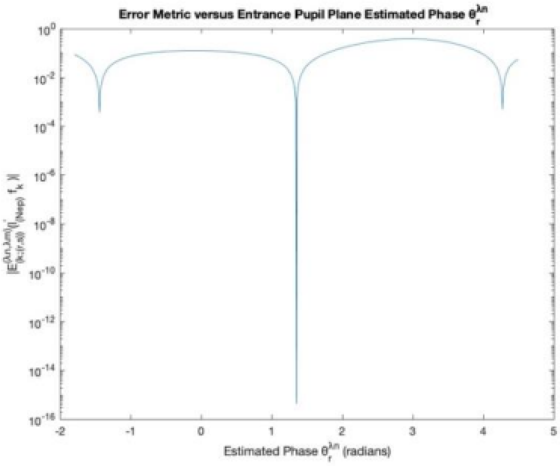

Figure 3 – Error function $E_{k;(r,s)}^{\lambda_n,\lambda_m}(l'_{(N)}, f_k)$ as function of unknown phase $\theta_r^{\lambda_n}$ over (-π, π].

Over the search space (x-axis in Figure 3), there are two other minimums shown with shallow wells (i.e., they reach small values but do not go to zero as seen by the true solution seen by the dip in Figure 3 between 1 and 2. To check this result, we generated a different error metric based on 3 separate wavelengths. This different error metric is shown in Figure 4 below and does not directly use the magnitudes of the irradiance

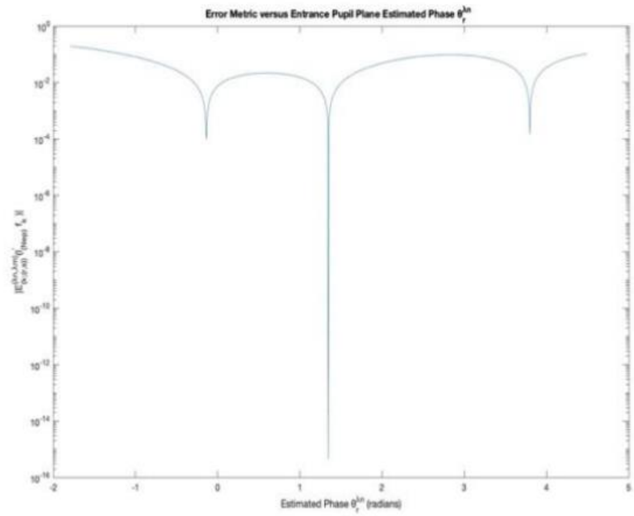

Figure 4 – Error function $E_{k;(r,s)}^{\lambda_n,\lambda_m}(l'_{(N)}, f_k)$ as function of unknown phase $\theta_r^{\lambda_n}$ its principal range.

spectra at different wavelengths. Instead, 3 separate irradiance spectrum ratios at different wavelengths are used, based on Equation (7), and combined in such a way as to zero the contribution of the unknown (as yet) object radiant emittance phase term $e^{j\phi_o^{\lambda_n}\left(l'_{(N_{ep})}, f_{l=k}\right)}$. The plot of the error metric in Figure 4 shows a clear, single minimum at $\theta_r^{\lambda_n} = 1.3464$ radians and exactly matches the reference (truth) phase used in generating the irradiance spectra measurements in our simulation, confirming our results using Equation (10). Two considerations with regards to implementing the error metrics shown in Figures 3 and 4 are, 1) the steep descent and narrow channel for the true solution, and 2) the two other local minima that lead to false results. Both considerations could impact the sampling strategy employed in the error minimization search algorithm and may require adaptive sampling methods to mitigate the chances of missing the true solution and settling on a false local minimum. Apart from employing adaptive sampling methods, some other potential solutions to this sampling issue may be to develop an alternate/complementary error metric, employ additional constraints, or search for an exploitable statistical feature in the physics of the propagating electromagnetic wave. We have already accomplished this as seen in the two different error metrics in Figures 3 and 4. Notice, that by using both different error metrics together, the false solutions can be directly eliminated by pointwise comparing these error metrics, since the false minimums occur at different phase estimate locations. In the future, it may also be useful to apply machine learning algorithms to atmospheric entrance pupil plane phase models like phases generated using the Von Karmen spectrum and/or the Kolmogorov spectrum to see if there are any exploitable hidden phase structural elements that can be used in combination with our approach to better estimate the object magnitudes or discriminate between local minima in the error metrics. We plan on investigating these options in the future.

The process to find the unknown entrance pupil plane phase values $\theta_r^{\lambda_n}$ and $\theta_s^{\lambda_n}$ is to use our developed 3 wavelength dependent error metric combined with our original error metric to eliminate the two false local minima. Note that between both these error metrics, only the true error solution goes to zero on both error metrics. By computing the error metric at all three minima, and comparing the results, the true minimum may be determined without an aggressive, adaptive sampling strategy.

Also, considering the conceptual model shown in Figure 2 with no aperture mask, the 1-point overlap result ($k = 1$) for the "no mask required" result in this work, uses the same approach and error metric as for the referenced masked methodology and provides the values of $\theta_i^{\lambda_n}$ and $\theta_j^{\lambda_n}$.[9] For the 2 – point overlap problem ($k = 2$), the complex constants $C_k^{\lambda_m}$ and $C_k^{\lambda_n}$ in Equation (10) are set to zero, and the object radiant emittance spectrum magnitudes are determined as mentioned above and substituted into Equation (10). The unknown phases $\theta_r^{\lambda_n}$ and $\theta_s^{\lambda_n}$ are discretized and searched over required combinations of their principal range values (-π, π], until the minimum error determines the correct values of $\theta_r^{\lambda_n}$ and $\theta_s^{\lambda_n}$. These values are then scaled to other wavelength ranges and the OTF can then be determined at all desired wavelengths. Once the OTF is determined at desired wavelengths, it can be inverted in accordance with Equation (1) to provide the atmospheric turbulence compensated object radiant emittance spectrum at the spatial frequency corresponding to $f2$. The determined values $\theta r\ \lambda n$ and $\theta s\ \lambda n$ for the 2-point problem along with $\theta i\ \lambda n$ and $\theta j\ \lambda n$ can be used in Equation (4) to determine the complex constants needed in the 3-point overlap problem using the 3-wavelength error metric discussed above. This process continues wherein the previous results are used to generate the complex constants needed in the OTF and error minimization expressions for the next overlap (i.e., next needed value of k). In this fashion, the entire linear spatial array for the image can be corrected for atmospheric turbulence with no diversity term, and only requiring three wavelengths. It must be stated that as the atmospheric state changes from realization to realization, the entrance pupil plane phases for previous results (i.e., entrance pupil plane phases associated with previous overlap results less than the current value of k) must be re-determined since the entrance pupil plane phases will change as the atmosphere changes. Consequently, this process is not real-time and can be computationally intensive. However, this approach has the advantage of 1) not requiring an entrance pupil plane mask, 2) does not require a diversity image[11] , and 3) can work with as few as 3 wavelengths and so is applicable to colored imagery, post processed color video, multi-spectral imaging cameras, and

HSI systems. For HSI systems, this method applies to all types of HSI sensors (i.e., single pixel scanners, push broom sensors, step-stair sensors, and systems that simultaneously capture the full HSI data cube. In the next section we present the results of the WOLF algorithm as applied to a multi-wavelength imaging system. As an example of the WOLF ATC algorithm working on a single wavelength of an image, as would be seen from a HSI system working in the spectral scanning mode of Figure 1 (2nd top-left image), or a normal monochromatic imaging camera, we see an image of Jupiter and its moon Europa on the left side of Figure 5. In this colored reference image Jupiter's moon Europa is clearly seen as a small bright dot on the left.

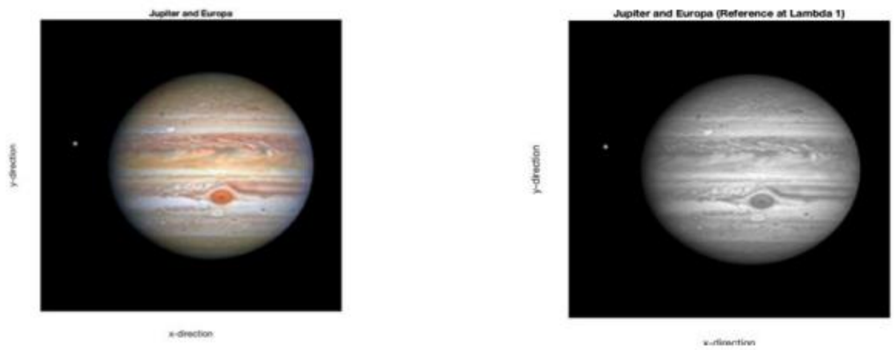

Figure 5 – Reference image of Jupiter and Europa (left) Courtesy of NASA, ESA, STScI, A. Simon (Goddard Space Flight Center), and M.H. Wong (University of California, Berkeley) and the OPAL team - https://hubblesite.org/contents/media/images/2020/42/4739-Image, Public Domain, https://commons.wikimedia.org/w/index.php?curid=95740740. Right image reference image at one wavelength.

To the right of Figure 5, we see a single wavelength representation of the colored image and Europa is still brightly visible as is expected in our reference (truth) monochromatic image. We apply simulated atmospheric turbulence to the reference image at λ_1 and apply a Von Karman atmospheric turbulence model with a maximum phase variation of 2π radians across the entrance pupil plane aperture, and that has the correct atmospheric turbulence statistics. Figure (6) shows the atmospheric turbulence degraded image for

Figure 6 – Simulated atmospheric turbulence degrade image irradiance at one wavelength (left). ATC (reconstructed image irradiance using the WOLF methodology (right).

the reference single wavelength HSI image irradiance (left), and the WOLF corrected image on the right side. Note that for the atmospheric turbulence degraded image on the left, Europa is much dimmer, and the image of Jupiter is much blurrier than the reference image. Note that when comparing the WOLF ATC image to the reference image, the WOLF ATC image restored the brightness of Europa and the spatial detail in the original image. The ATC simulation used a 127 x 127 sampled entrance pupil plane aperture corresponding to an OTF with 253 x 253 pixels at any given wavelength. The push broom HSI system would produce a slice of spatial data that is 253 pixels long and would produce an arbitrary number of wavelengths at each pixel. Only 3 distinct wavelengths are required for our approach resulting in our approach being valid for general 3-color imaging systems like digital RGB cameras, but arbitrarily large numbers of wavelengths can conceptually be corrected if the imaging system captures the spectral irradiance values associated with the OTF at all relevant spatial frequencies and all applicable wavelengths. With regards to the imaging system itself, considerations such as a low noise design; proper sampling so that there is no aliasing; setting the sensor integration times so that there is sufficient signal at each detector pixel to run the WOLF ATC algorithms but also ensuring that each image realization does not violate Taylor's frozen flow approximation; ensuring that the aperture size is larger than the atmospheric coherence length (Fried parameter) r_o so that the ATC process will produce noticeable results[12]; and ensuring that the correct image segment is within the isoplanatic angle so that the ATC correction is not applied to too large of an image segment; must be considered in the development of the imaging system.

SUMMARY

We have developed a method for atmospheric turbulence compensation using the WOLF ATC methodology that does not require a diversity-based imaging system to carry out ATC on captured imagery. Additionally, the methods outlined above do not require any specialized hardware for ATC such as simultaneously captured image pairs (in-focus image and diversity image with different optical path length), or entrance pupil plane aperture masks, and just requires an imaging system configuration capable of capturing images at 3 colors at all spatial camera pixels. The approach scales to an arbitrarily large number of wavelengths and a notional push broom HSI imaging system was used to illustrate our concepts, although other HSI implementations are equally valid.[13] We developed a two-stage approach that first estimates the object spectrum magnitude at all required spatial frequency locations, and then used this information to estimate the corresponding OTF and subsequent object spectrum at all required spatial frequencies. We developed the mathematical framework and illustrated our results with a representative simulated push broom HSI system that had 253 spatial frequency sensing elements in a linear array, and which was zero-packed to 256 pixels. The array was scanned through 256 lines producing a 2D spatial image map of 256 x 256 pixels. Only 3 wavelength elements at each pixel were required for our adapted WOLF algorithm. In removing the requirement for a diversity image, and making the ATC process a software-only, instead of a software-dominant process, we had to give up the real-time capable aspects of the WOLF methodology in this adaptation. This is because in the first part of our two-stage adaptation of the WOLF methodology, a series of separate atmospheric realizations are required to determine the estimate of the object magnitude spectrum at relevant spatial frequencies and wavelengths. To capture high quality images and benefit from the application of ATC, the entrance pupil plane aperture must be larger than the atmospheric coherence length (Fried parameter). The entrance pupil plane aperture element is typically the primary mirror in a telescopic imaging system and the spatial resolution increase that the ATC imaging system can achieve is D_{ep}/r_0, where D_{ep} is the diameter of the entrance pupil (primary mirror) and r_0 is the Fried parameter. The ATC imaging system must also have proper spatial sampling so that there is no aliasing and sufficient per pixel signal-to-noise ratio (SNR) at the detector so that the WOLF algorithms have sufficient signal to carry out the ATC process. A rule of thumb is a per pixel detector SNR of 10 is a good guideline although smaller SNRs have shown reasonable results. Additionally, the integration time on the optical imaging system needs to freeze the atmosphere and so cannot exceed a few milliseconds. We used 2 *ms* in our study. An interesting side note is that if imaging data has been captured that satisfies these criteria (to include at 3 simultaneous distinct wavelengths for each pixel and have many atmospheric realizations/image frames at separate wavelengths and different atmospheric states), then the adapted WOLF ATC method can be applied to historical data sets to remove the atmospheric turbulence and increase the spatial resolution to the near diffraction-limited state. For spectral imaging sensors (multi-spectral, hyperspectral, and ultra-spectral) these methods can also provide a better spectral characterization by removing the aberrations for each wavelength at each pixel (if the spectral irradiance spectrum is captured for each corrected wavelength at each pixel).

REFERENCES

1. Roddier, François. “The effects of atmospheric turbulence in optical astronomy.” Progress in optics. Vol. 19. Elsevier, 1981. 281-376.
2. Tyson, Robert K., and Benjamin West Frazier. Principles of adaptive optics. CRC press, 2022.
3. Ellerbroek, Brent L. "First-order performance evaluation of adaptive-optics systems for atmospheric-turbulence compensation in extended-field-of-view astronomical telescopes." JOSA A 11.2 (1994): 783-805.
4. R. A. Johnson, "Introduction to Adaptive Optics," in Fundamentals of Adaptive Optics, Springer, 2004, pp. 1-27.
5. William W Arrasmith. High-speed diversity-based imaging method for parallel atmospheric turbulence compensation, May 21 2013. US Patent 8,447,129.
6. W. Arrasmith. "Diversity-based atmospheric turbulence compensation for incoherent imaging systems using a new well optimized linear finder methodology," Universal Journal of Lasers, Optics, Photonics & Sensors, Vol. 2 Issue No. 1 – June 2021.
7. "Acquisition Techniques for Hyperspectral Imaging". Wikimedia Commons, 26 June 2015, https://commons.wikimedia.org/wiki/File:AcquisitionTechniques.jpg. Accessed 29 April 2023.
8. Goodman, Joseph W. Introduction to Fourier optics. Roberts and Company publishers, 2005.
9. W. Arrasmith, E. He. "Generalizing the Well-Optimized Linear Finder (WOLF) Atmospheric Turbulence Compensation (ATC) Methodology to non-Diversity based Imaging Systems using Entrance Pupil Plane Aperture Masks," Universal Journal of Lasers, Optics, Photonics & Sensors, Vol. X Issue No. Y – June 2023. (Submitted)
10. Goodman, Joseph W. Statistical optics. John Wiley & Sons, 2015.
11. Robert A Gonsalves. Phase retrieval and diversity in adaptive optics. Optical Engineering, 21(5):215829, 1982.
12. M. C. Roggemann, B. Welsh, Imaging Through Turbulence, CRC Press, New York, 1996.
13. Yokoya, N., Yoneyama, A., & Takahashi, T. (2009). Hyperspectral imaging system with switchable spectral filter array. Optical Engineering, 48(6), 063201.